Technical Sciences
Academy of Romania
www.jesi.astr.ro

Journal of Engineering Sciences and Innovation
Volume 10, Issue 2 / 2025, pp. 153 - 166

C. Chemical Engineering, Materials Science and Engineering

Received ***24 January 2025*** *Accepted* ***10 June 2025***
Received in revised form ***10 Apryl 2025***

A Lysosome-Targeted Ruthenium (II) photosensitizer for enhanced immunogenic cell death

HANXUE LIU[1], JIANCHUN JIANG[1], MENG REN[1], XIANGYU DAI[1], ZHENGQI SHEN[1], XULING XUE[1], DUMITRA LUCAN,[2] NAI-XING WANG[3], HONG-KE LIU[1]**

[1]School of Chemistry and Materials Science, Nanjing Normal University, Nanjing 210023, China
[2]Technical Sciences Academy of Romania ASTR, Dacia Avenue no.26, Bucharest, Romania
[3]Technical Institute of Physics and Chemistry &, University of Chinese Academy of Sciences, Chinese Academy of Sciences, Beijing, 100190 China

Abstract. Photoactivated immunogenic cell death (ICD) boosts immune responses but faces challenges. Here we present a 2,2'-bipyridine ruthenium complex **Ru-LND** as a photoactivated ICD inducer, which demonstrated favorable efficacy in inhibiting MCF-7 cell proliferation upon photoactivation. **Ru-LND** significantly increased cytotoxicity, particularly against 3D multicellular tumor spheroids, and synergistically enhenced the immune regulatory response within tumors by employing multiple mechanisms including precise lysosomes localization, mitochondrial dysfunction, RIPK3 and MLKL mediated necroptosis and reactive oxygen species (ROS) generation. This study introduced the first 2,2'-bipyridine ruthenium-based photosensitizer, unveiled a novel anticancer mechanism through photoactivated antitumor complex that induced ICD, and thus offering a new therapeutic approach to boost the efficacy of photo-immunotherapy for cancer treatment.

Keywords: 2,2'-bipyridine Ruthenium Complex; Lysosome Targetability; Photodynamic Therapy; Immunogenic Cell Death; Anticancer.

1. Introduction

Photo-driven cancer therapies have garnered increasing attention. The development and design of photoactivated complexes represent a novel strategy and hot topic in the field of antitumor complex research[1, 2]. Compared to traditional chemotherapy,

*Correspondence address: liuhongke@njnu.edu.cn

photoactivated antitumor complexes possess several unique advantages, including controllable activation in time and space, no cross-resistance with chemotherapeutic drugs, and minimally invasive nature[3]. Recent studies have indicated that, in addition to their direct tumor-destructive capabilities, some photoactivated complexes can also induce immunogenic cell death (ICD) in tumor cells[4].

In recent years, it has been discovered that photoactivated antitumor complexes primarily induce ICD by generating reactive oxygen species (ROS) and singlet oxygen ($^1O_2$). For instance, Tan reported an iridium(III) photosensitizer (**IrFc1**) containing a ferrocene group, which catalyzes the production of $^1O_2$ and hydroxyl radicals (·OH) through an autocatalytic process, inducing ferroptosis and leading to immunogenic cell death in tumor cells[5]. Brabec synthesized four iridium(III) complexes with a benzimidazole framework that produce ROS upon photoactivation, damaging cellular organelles and DNA, thereby inducing ICD[6]. Our group synthesized a new type of near-infrared photosensitizer **Ir-1**, which utilizes its ability to generate ROS under light exposure to cause lysosome-dependent cell death (autophagy blockage and mitochondrial apoptosis), activating immunogenic cell death[7].

Some studies have also found that photoactivated antitumor complexes can induce ICD through pyroptosis or ferroptosis pathways. Mao reported two iridium(III)-triphenylamine photosensitizers (**IrC** and **IrF**) that induce typical pyroptosis and ferroptosis simultaneously, enhancing the immune activation of antitumor therapy[8]. Chao synthesized a mitochondria-targeting iridium(III) photosensitizer **Ir-pbt-Bpa**, which activates immunogenic cell death by generating ROS and inducing ferroptosis[9].

In addition to this, photoactivated antitumor complexes can also induce ICD by targeting specific parts of tumor cells, such as nucleoli. For example, Zhu reported a new photo-caged, water-soluble, and nucleolar-targeting Pt(IV) prodrug, which accumulates and converts to oxaliplatin in the nucleolus through a photoactivation mechanism, causing DNA damage, cellular senescence, and p53-independent cell death, while activating ICD and ultimately triggering an immune response[10].

Nevertheless, due to the unclear targeting and photoactivation mechanisms of photoactivated antitumor complexes, there are not many complexes that can produce an excellent photoactivated immune effect[1, 11-13]. Ruthenium complexes containing 2,2'-bipyridine (for example, $[Ru(bpy)_3]^{2+}$) typically exhibit excellent photophysical properties, good water solubility, and a structure that is easy to modify, making them ideal candidates for photosensitizers[14]. Additionally, $[Ru(bpy)_3]^{2+}$ has a high quantum yield and strong fluorescence signal, serving as a fluorescence probe for biosensors and optoelectronic devices, and as a luminescent substrate for electrochemiluminescent immunoassays[15]. However, up to date, there have been no reports of photoactivated 2,2'-bipyridine ruthenium-based antitumor complexes inducing ICD.

Basing on previous works, we have proposed a metal-ligand synergistic enhancement (MLSE) strategy that combines metal centers with natural products or

active molecules. By selecting metals and organic precursors with specific functions and modes of action, the activity of the complexes can be greatly enhanced, and new mechanisms of action can be demonstrated[16, 17]. Lonidamine is a broad-spectrum antineoplastic drug used in the treatment of various tumors, especially breast cancer[18]. Although Lonidamine itself does not have high anticancer activity; its main mechanism of action targets the unique glycolytic pathway in tumors, disrupting cancer cell metabolism, reducing cancer cell oxygen consumption, and producing more ROS for photodynamic therapy (PDT), as well as affecting the expression of apoptosis-related proteins to kill tumor cells[19]. In this study, we designed and synthesized a lysosome-targeting photosensitizer **Ru-LND** with high phototoxicity to breast cancer MCF-7 cells by introducing Lonidamine into 2,2'-bipyridine ruthenium(II). **Ru-LND** specifically targets lysosomes, generates a high yield of ROS, significantly disrupts mitochondrial function, upregulates key necrosis proteins RIPK3 and MLKL, induces necroptosis as well as the release of CRT (calreticulin), HMGB1 (high-mobility group box 1), and ATP, enhancing the immune activation of antitumor therapy. Furthermore, **Ru-LND** significantly inhibited the growth of three-dimensional cell spheroids, demonstrating potential for the treatment of solid tumors. This paper reported the first photosensitizer based on 2,2'-bipyridine ruthenium(II) that induces tumor immunogenic death through necroptosis via targeting lysosomes. This study not only discovered a new anticancer mechanism of inducing ICD by photoactivated antitumor complexes, but also provided a new perspective for the development of photoactivated antitumor complexes.

2. Results and discussion

2.1. Synthesis and photophysical properties of the complexes

Ligand L2 was synthesized via an amidation reaction between lonidamine and the organic ligand 1,10-phenanthroline-5-amine (L1). The metal complex **Ru-LND** was subsequently obtained by coordinating ligand L2 with the metal precursor cis-$[Ru(bpy)_2Cl_2]\cdot 2H_2O$ (Fig. 1). The control complex **Ru-NH₂** was prepared by directly coordinating 1,10-phenanthroline-5-amine with $[Ru(bpy)_2Cl_2]\cdot 2H_2O$ (Scheme S1). Structural characterization of **Ru-LND** was carried out using proton nuclear magnetic resonance (^{1}HNMR) spectroscopy and electrospray ionization mass spectrometry (ESI-MS), as presented in Figure. S1-S3.

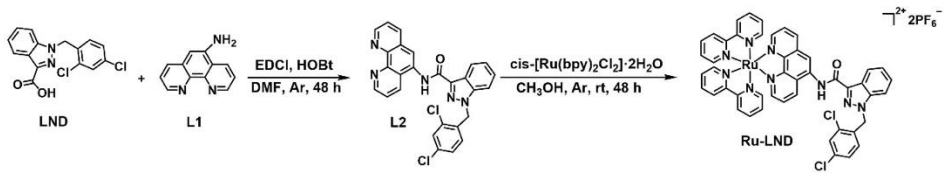

Fig. 1. Synthesis routes for complex **Ru-LND**.

The lipophilicity of the anticancer agents, which affected the capacity to traverse the cell membrane and thus its pharmacological activity, can be quantified by determining partition coefficient (Log $P_{o/w}$) values between organic solvent and water. As shown in Figure. S4, the Log $P_{o/w}$ values for LND and **Ru-NH₂** are ~1.51 and 1.81, respectively. In comparison, **Ru-LND** exhibited significantly enhanced lipophilicity, with a Log $P_{o/w}$ value of ~2.71. This increased lipophilicity suggests that **Ru-LND** might have a higher tendency to enter cells and more readily participate in intracellular processes.

The photophysical properties of the complexes were evaluated through UV-Vis absorption and fluorescence spectroscopy (Figure. S5). Both **Ru-LND** (10 μM) and **Ru-NH₂** (10 μM) exhibited similar spectra with strong UV-vis absorption peaks at 450 nm, except that the absorption intensity of **Ru-LND** is slightly higher than that of **Ru-NH₂**. Notably, **Ru-LND** displayed a distinct fluorescence emission at 625 nm with the excitation of 450 nm, of which approximately 1.28 times higher than that of **Ru-NH₂**. The observed differences in intensity of UV-vis and fluorescence emission behavior are likely attributed to the incorporation of lonidamine, which altered the metal-to-ligand charge transfer (MLCT) properties of **Ru-LND**[14]. Besides, we further detected the photostability of **Ru-LND** under light irradiation (450 nm, 3.5 mW cm^{-2}), both **Ru-LND** and **Ru-NH₂** demonstrated minimal shifts in their absorption spectra (Figure. S6), highlighting the robustness against photodegradation.

We employed the 1,3-Diphenylisobenzofuran (DPBF) as the selective probe known for its specificity towards $^1O_2$ species by monitoring the decrease of the absorbance intensity at about 410 nm[20]. Our experimental findings reveal that upon exposure to 450 nm irradiation, both **Ru-LND** and the precursor **Ru-NH₂** demonstrated time-dependent degradation at its distinctive absorption peak at ~416 nm indicating their high $^1O_2$ yield under light irradiation (Figure. S7). Comparisons with commercial probes revealed that **Ru-LND** exhibited a higher yield of singlet oxygen species compared to $[Ru(bpy)_3]Cl_2 \cdot 6H_2O$, indicating that the complex could serve as an excellent photosensitizer for photodynamic therapy in cancer treatment.

We further investigated the oxidation of NADH by ROS. As depicted in Figure. S7, no significant reduction was observed at absorbance of 340 nm when the ligand LND was co-incubated with NADH under light exposure, indicating that the ligand does not oxidize NADH. However, NADH exhibits a time-dependent decrease in absorbance at 340 nm upon interaction with **Ru-LND** in light condition, a similar phenomenon was also observed in **Ru-NH₂** group. This observation suggests that both complexes have the capacity to oxidize NADH, which could potentially disrupt cellular redox homeostasis.

2.2. Cytotoxicity *in vitro*

The MTT assay was employed to assess the cytotoxicity of **Ru-LND** under 450 nm light-irradiation for 15 min, with LND, the metal precursor **Ru-NH₂** and Cisplatin

as comparative control groups. The cytotoxicity assessments were conducted on a panel of cancer cell lines, including MCF-7, MDA-MB-231, HeLa, and A549 cells. As shown in Table 1, the control compounds LND (IC_{50}>100 μM) and **Ru-NH₂** (IC_{50}>50 μM) exhibited non-toxic under both light exposure and dark conditions, while Cisplatin showed high cytotoxicity under both conditions. In contrast, **Ru-LND** demonstrated minimal to moderate toxicity towards MCF-7, MDA-MB-231, A549, and HeLa cells in dark condition, with IC_{50} values ranging from ~24.3 to ~103.5 μM. Upon 15 min-light irradiation, **Ru-LND** displayed significant phototoxicities against all the tested cancer cell lines, with the IC_{50} values on MDA-MB-231, A549 and HeLa cells approximately ~14.8 μM, ~6.9 μM, and ~6.9 μM, respectively. It is also noteworthy that **Ru-LND** exhibits a higher phototoxicity against the MCF-7 cells compared to cisplatin, with an IC_{50} value of ~5.2 μM. The phototoxicity index (PI) was found to be as high as ~16.3 times under light irradiation than the dark condition, signifying a substantial enhancement in cytotoxicity upon light exposure. Moreover, **Ru-LND** displayed greater cytotoxicity than **Ru-NH₂** under light conditions, which might be attributed to its enhanced lipophilicity. Based on these findings, MCF-7 cells were selected as a model system for further investigation into the mechanisms underlying the cytotoxic action of **Ru-LND** under light exposure.

Table 1 IC_{50} values for LND, **Ru-NH₂**, **Ru-LND** and Cisplatin against several cancer cell lines for both in dark and light (the cell lines were incubated in the dark for 6 h, and then subsequently irradiated with 450 nm light for 15 min, 3.5 mW·cm^{-2}) conditions.

Compound		IC_{50} values (μM) towards different cell lines for 48 h			
		MCF-7	**MDA-MB-231**	**A549**	**Hela**
LND	Dark	>100	>100	>100	>100
	Light	>100	>100	>100	>100
Ru-NH₂	Dark	>100	>100	>100	>100
	Light	>50	>100	>50	>100
Ru-LND	Dark	84.9±0.3	24.3±0.4	65.3±0.1	103.5±0.4
	Light	5.2±0.1	14.8±0.1	6.9±0.1	6.9±0.2
	PI	16.3	1.6	9.5	15.0
Cisplatin	Dark	7.6±0.1	32.4±0.1	5.6±0.7	9.0±0.5
	Light	8.1±0.2	30.1±0.2	5.9±0.2	9.5±0.3
	PI	0.9	1.1	0.9	0.9

The PI (phototoxicity index) was the ratio between the IC_{50} values in the dark upon light irradiation.

2.3. Mitochondrial dysfunction induced by Ru-LND

Based on the above results that **Ru-LND** has a high capacity for generating singlet oxygen species in solution, we further assessed the production of intracellular ROS using the fluorescent probes H_2DCFDA by laser confocal microscopy (CLSM) and flow cytometry. As shown in Fig. 2a, the control groups (LND and **Ru-NH₂**) exhibited no green fluorescence in the absence of light, except that a faint DCF fluorescence signal was discernible within the **Ru-LND** treated group. Upon exposure to 450 nm light, a pronounced green fluorescence signal was observed in

MCF-7 cells treated with **Ru-LND** (15 μM), indicative of elevated ROS levels. However, only weak green fluorescence was produced after treatment with **Ru-NH₂**. Quantitative analysis by flow cytometry revealed that this enhancement occurred in a concentration-dependent manner, with ROS levels peaking at approximately threefold of the **Ru-NH₂** treatment group at the same concentration (Fig. 2b-c). This validated that **Ru-LND** could significantly generate ROS in vitro upon short time of photoactivation, reinforcing its potential as a promising photosensitizer for PDT applications.

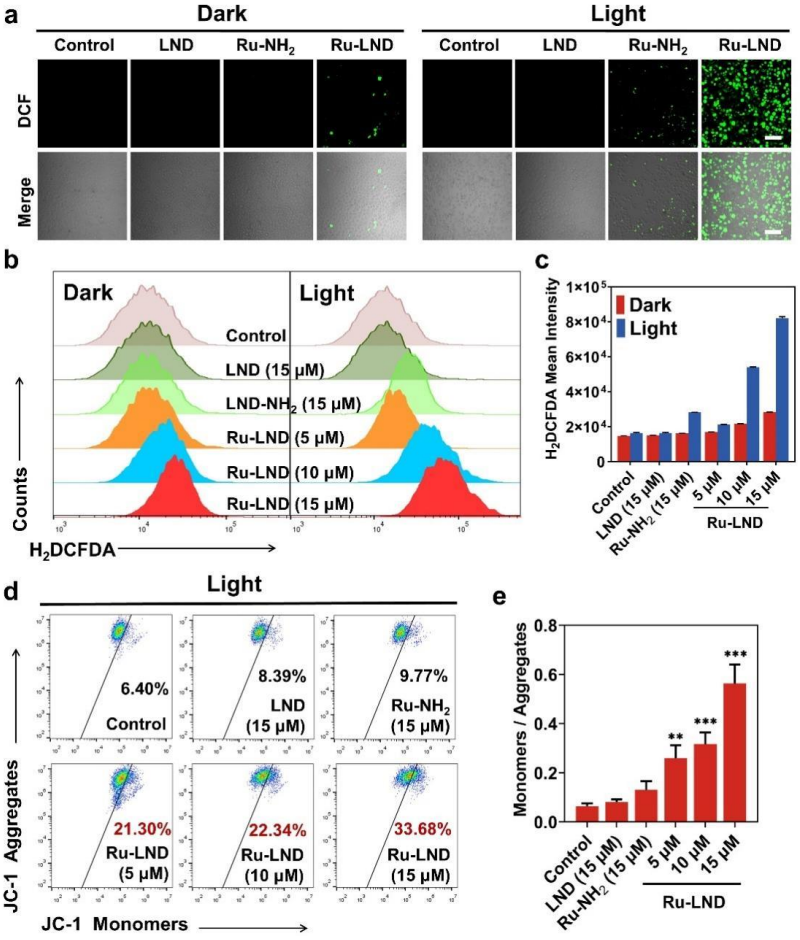

Fig. 2. **Ru-LND** induced ROS and mitochondrial disfunction in MCF-7. a) In the dark and under 450 nm light illumination (3.5 mW cm^{-2} for 15min), confocal fluorescence images of MCF-7 cells for the total ROS production after the treatments with LND (10 μM), **Ru-NH₂** (10 μM), **Ru-LND** (10 μM) with H_2DCFDA (10 μM). Scale bar: 100 μm. b-c) Flow cytometry quantitatively detects the levels of ROS in MCF-7 cells before and after different treatments under light exposure. d) Flow cytometry quantification of JC-1-labeled MCF-7 cells treated with different concentrations of LND (15 μM), **Ru-NH₂** (15 μM), **Ru-LND** (5 μM, 10 μM, 15 μM) with irradiation (450 nm, 3.5 mW cm^{-2}) for 15 min. e) The quantitative analysis for the ratio of JC-1 monomers to JC-1 aggregates in MCF-7 cells. Monomers: λ_{ex} = 490 nm, λ_{em} = 530 nm; Aggregates: λ_{ex} = 525 nm, λ_{em} = 590 nm. Error bars: S.D., n = 3. **p < 0.01, ***p < 0.001.

The flow cytometry analysis displayed the proportion of JC-1 aggregates in the mitochondria was high in all the groups blank, LND, **Ru-NH₂** and **Ru-LND** in the dark condition, indicating a high mitochondrial membrane potential (Figure. S8). After exposure to light, no substantial differences in MMP were observed in the control (blank, LND and **Ru-NH₂**) groups. In contrast, the ratio of JC-1 monomers to aggregates gradually increased from ~6.40% to ~33.68% as the drug concentrations of **Ru-LND** increase from 5 to 15 μM (Fig. 2d-e), indicating a significant decrease in mitochondrial membrane potential of MCF-7 cells.

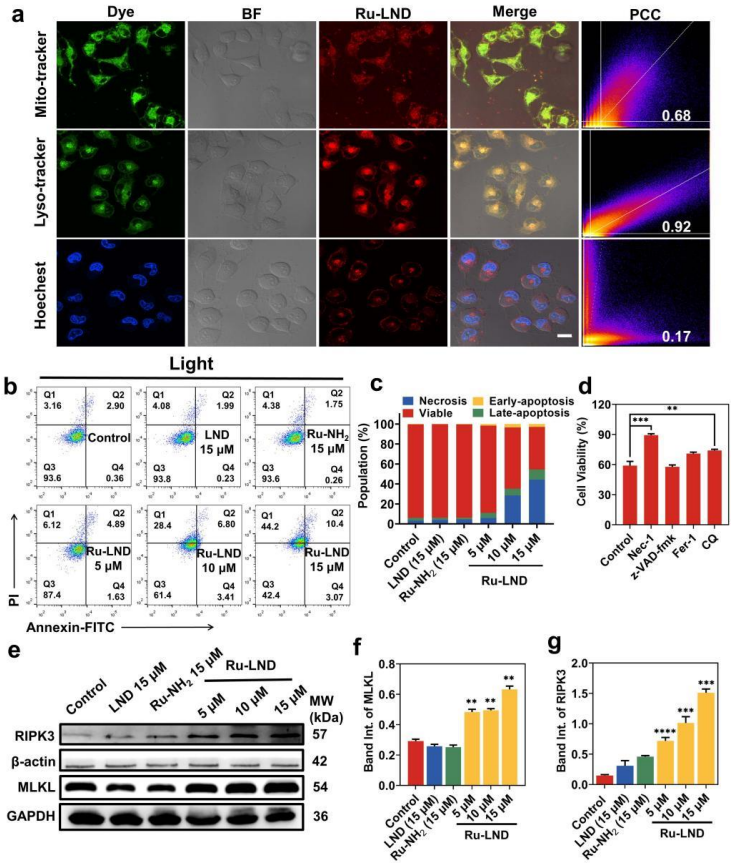

Fig. 3. The cell death mechanism after **Ru-LND** treatment. a) Subcellular distribution confocal study of **Ru-LND** (10 μM) MCF-7 cells by co-localization imaging with Mito-Tracker Green (0.2 μM) or Lyso-Tracker Green (2 μM), and Hoechst (1 μM). Scale bar: 20 μm. b) Flow cytometry assays of Annexin V-FITC/PI-labeled MCF-7 cells in LND (15 μM), **Ru-NH₂** (15 μM), **Ru-LND** (5 μM, 10 μM, 15 μM) for 24 h, under 450 nm light irradiation for 15 min. c) Quantitative analysis of cell apoptosis. d) Cell viability of MCF-7 cells determined upon co-incubation (48 h) with different concentrations of **Ru-LND** and different inhibitors. The inhibitors Fer-1 (10 μM), z-VAD-fmk (25 μM), Nec-1 (50 μM), and CQ (50 μM) were administrated 1 h before co-incubation with Ru-LND, under 450 nm light irradiation for 15 min. e) Expressions of RIPK3 and MLKL in MCF-7 cells treated with LND (15 μM), **Ru-NH₂** (15 μM), **Ru-LND** (5 μM, 10 μM, 15 μM) for 48 h, respectively. f, g) quantitative analysis of the expression of RIPK3 and MLKL proteins. Error bars: S.D., n = 3. $^{**}p < 0.01$, $^{***}p < 0.001$, $^{****}p < 0.0001$.

2.4. Determination of the cell death mechanism

Furthermore, we detected the cell death mechanism of MCF-7 cells after treatment of **Ru-LND** in light conditions. As is reported the intracellular distribution of the drug has a significant impact on the cell death mechanism, thus we determined the localization in MCF-7 cells of **Ru-LND** utilizing CLSM, by employing commercially available fluorescent dyes (Lyso Tracker Green, Mito Tracker Green and Hoechst 33342).

Fig. 3a illustrates a pronounced overlap between the red fluorescence of **Ru-LND** and the green fluorescence of lysosomes, with a high co-localization coefficient of ~0.92. A moderate overlap was observed with mitochondria, with a coefficient of ~0.68, while the weakest correlation was found in the cell nuclei, with a coefficient of ~0.17. This suggests that **Ru-LND** exhibits a preference for accumulation within lysosomes, a phenomenon potentially linked to lysosomal dysfunction. Such dysfunction can trigger a cascade of biological consequences, notably the upregulation of receptor-interacting protein kinases (RIPKs), which are pivotal in the regulation of cell death and inflammatory pathways, and thus influential in the process of necroptosis[21].

Then we investigated the cell death mechanisms induced by **Ru-LND** upon irradiation with 450 nm light through flow cytometry and WB assays, etc. Figure. S9 depicts that both the control and **Ru-NH$_2$**, as well as **Ru-LND**-treated cells exhibited no significant signs of apoptosis, remaining in the region characteristic of normal cells in the absence of light. However, there was a notable shift in the **Ru-LND**-treated cells towards region Q1 in a dose-dependent manner upon light exposure from ~2.36% (0 μM) to ~44.2% (15 μM), indicative of necrosis cells (Fig. 3b-c). While treatment with **Ru-NH$_2$** did not manifest this phenomenon, demonstrating that **Ru-LND** can efficiently induce necroptosis in cells when exposed to light. Besides, the cell survival rates were detected by pre-incubating with various cell death inhibitors. As shown in Fig. 3d, the survival rates of MCF-7 cells treated with the necroptosis inhibitor Nec-1 increased significantly to 88% from ~59% in the control group, respectively. This suggested that the mode of cell death induced by **Ru-LND** is primarily necroptosis. Moreover, we confirmed the induction of cell necroptosis by **Ru-LND** using WB assays by detecting the changes in the expression levels of necroptosis-related proteins such as RIPK3 and MLKL[22, 23]. As shown in Fig. 3, **Ru-LND** could elevate RIPK3 and MLKL protein levels in a dose-dependent manner upon light exposure (Fig. 3e-g), while the control (blank, LND and **Ru-NH$_2$**) groups could not influence the expression levels of RIPK3 and MLKL proteins, again confirmed the necroptosis mechanism of MCF-7 cells.

2.5. ICD effect induced by Ru-LND in tumor cells

As shown in Fig. 4a, confocal fluorescence imaging results revealed that the LND, **Ru-NH$_2$**, and **Ru-LND** groups all showed nodetectable green fluorescence from

CRT in the absence of light exposure. Notably, upon irradiation of the **Ru-LND** group, there was a marked enhancement in the green fluorescence emitted by the CRT antibody. In contrast, the LND and **Ru-NH$_2$** groups failed to exhibit any CRT fluorescence signals even under light exposure. Flow cytometric results further confirmed that **Ru-LND** could release CRT under light exposure and show a concentration-dependent trend (Fig. 4b-c), demonstrating that **Ru-LND** promotes the exposure of CRT on the surface of the MCF-7 cell membrane.

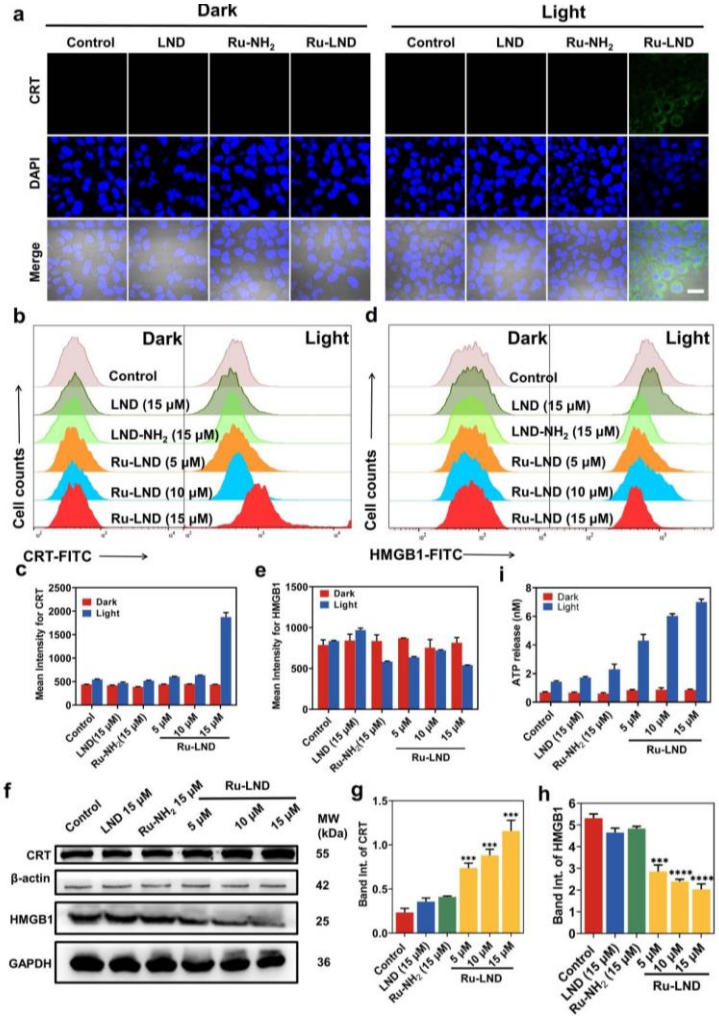

Fig. 4. **Ru-LND** induced immune activation in MCF-7 cells. a) Confocal images of CRT release in MCF-7 cells incubated with LND, **Ru-NH$_2$**, **Ru-LND** for 24 h. Scale bar: 25 μm. b, d) flow cytometry quantification of CRT and HMGB1 in MCF-7 cells after 24 h treatment upon dark and 450 nm irradiation (3.5 mW cm^{-2} for 15min) with LND (15 μM), **Ru-NH$_2$** (15 μM), **Ru-LND** (5 μM, 10 μM, 15 μM). c, e) Quantitative analysis of mean intensity for CRT and HMGB1. f-h) The immunoblotting and quantitative analysis of CRT and HMGB1. i) Analysis of extracellular ATP level in MCF-7 cells after treatment with LND (15 μM), **Ru-NH$_2$** (15 μM), **Ru-LND** (5 μM, 10 μM, 15 μM) for 24 h, irradiated with 450 nm light at a light power density of 3.5 mW cm^{-2} for 15 min. Error bars: S.D., $n = 3$. ***$p < 0.001$, ****$p < 0.0001$.

Analysis of HMGB1 release levels using flow cytometry revealed that the fluorescence signal associated with HMGB1 labeling showed no significant variation when LND, **Ru-NH$_2$**, and **Ru-LND** were incubated in the dark, and the intensity remained constant even with increasing concentrations of **Ru-LND**. Upon exposure to 15 min-light irradiation at 3.5 mW cm^{-2} (Fig. 4d-e), the enhanced fluorescence of HMGB1 suggests that **Ru-LND** can influence the release of HMGB1 with a concentration-dependent trend (5-15 μM). It is worth mentioning that the control complex **Ru-NH$_2$** could also induce the release of HMGB1 at high concentration condition (15 μM). This suggests that both **Ru-NH$_2$** in high concentration and **Ru-LND** are capable of facilitating the release of HMGB1 into the extracellular environment of cancer cells under light irradiation. Protein immunoblotting analysis provided further evidence that **Ru-LND** facilitated the release of CRT and HMGB1 following exposure to light for 15 min (Fig. 4f-h). In addition, an ATP detection kit was employed to quantify the levels of extracellular ATP in the cell supernatant. As shown in Fig. 4i, there was no variation in the ATP levels in the cell supernatants after drug treatment under dark condition, either in the control groups or **Ru-LND** group. Upon 15 min-irradiation, 15 μM **Ru-NH$_2$** group caused a slight change with 1.6-fold increase in ATP levels compared to the control group without treatment. In contrast, the **Ru-LND**-treated group induced a significant 5.0-fold increase in ATP release in a concentration-dependent manner. Collectively, these results indicate that **Ru-LND** could effectively induce ICD under light exposure, highlighting its potential as a therapeutic agent for activating the immune response against cancer.

2.6. 3D tumor spheroids viability assays

To evaluate the inhibitory effects of **Ru-LND** on the growth of solid tumors, we employed a 3D spheroid model derived from MCF-7 cells. During a 7-day observation period, the size of tumor spheroids in the control group only light but without drug treatment exhibited an increasing trend by approximately ~1.15 times, with their diameter expanding from 607 μm to 699 μm. The other two control groups (**Ru-NH$_2$** and LND) after 450 nm irradiation for 15 min also exhibited a similar trend with the size of the cell spheroids gradually increasing by approximately ~1.06 times. In contrast, the **Ru-LND**-treated group showed a notable reduction in tumor volume with the diameter decreasing from 746 μm to 526 μm with ~1.42-time decrease (Fig. 5a-b), representing an approximate 1.42-fold decrease. This indicated that **Ru-LND** could significantly inhibit the growth of 3D cell spheroids. Furthermore, the live-dead staining assays were conducted to confirm the ability of **Ru-LND** to kill the cell spheroids. As shown in Fig. 5c, All the control groups (the control group that received only light exposure without drug treatment, LND-treated group and **Ru-NH$_2$**-treated group) exhibited green fluorescence, indicating intact cell membranes and vigorous metabolic activity, which are hallmarks of a viable state. Conversely, the tumor spheroids treated with **Ru-LND** exhibited intense red fluorescence, suggesting that the cells had ceased

their vital functions and transitioned to a state of necrosis. This pronounced shift in fluorescence from green to red not only underscores the cytotoxic impact of **Ru-LND** treatment but also indicates its potential in combating tumors. Collectively, these findings suggest that **Ru-LND** could effectively suppress the proliferation of 3D multicellular tumor spheroids derived from MCF-7 cells, demonstrating significant promise for clinical utility.

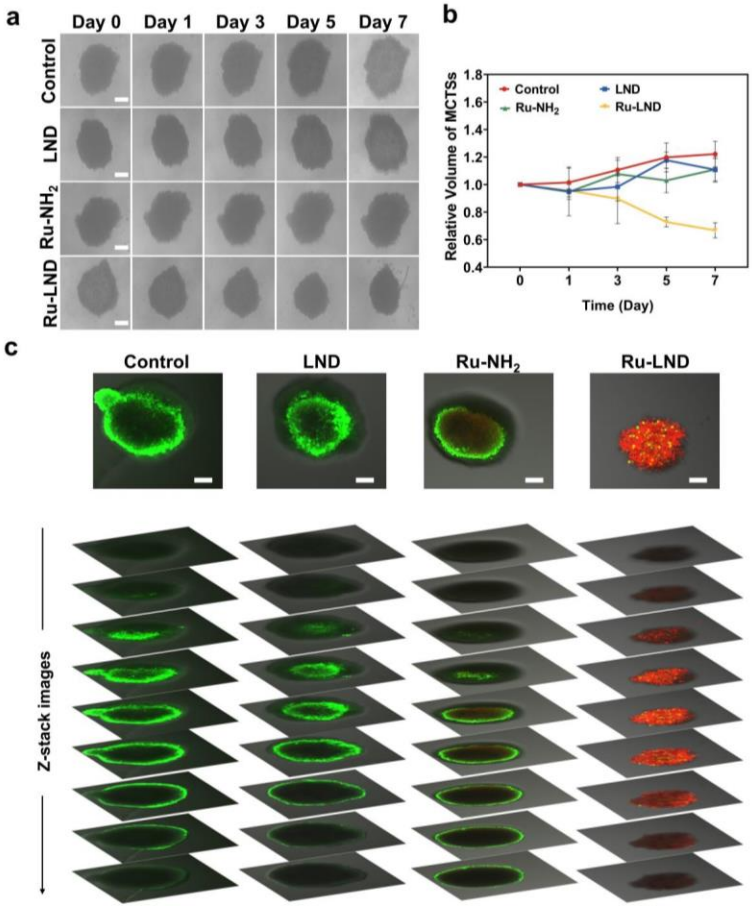

Fig. 5. The potent anti-tumor activity towards 3D MCF-7 tumor cell spheroid models. a) Representative images of 3D tumor spheroids after being treated with LND (50 μM), **Ru-NH₂** (50 μM), **Ru-LND** (50 μM) for 7 days. Scale bar: 200 μm. b) 3D spheroid growth spheroid diameter statistics of MCF-7 cells. c) Confocal images of the live/dead cells in the tumor spheroids after treatment with for 7 days, stained by Calcein AM/PI. Calcein AM: λ_{ex} = 490 nm λ_{em} = 515±20 nm; PI: λ_{ex} = 535 nm λ_{em} = 617±20 nm; Scale bar: 250 μm. Error bars: S.D., n = 3.

3. Conclusions

In summary, we have successfully synthesized **Ru-LND** by introducing lonidamine into 2,2'-bipyridine ruthenium. The results indicated that, compared to the control complex **Ru-NH₂**, **Ru-LND** exhibited very good phototoxicity. Upon

photoactivation, **Ru-LND** efficiently produced ROS, leading to mitochondrial dysfunction. **Ru-LND** specifically targeted lysosomes, significantly disrupts mitochondrial function, upregulates key necrosis proteins RIPK3 and MLKL, induced necroptosis, and released DAMPs such as CRT, HMGB1, and ATP. These mechanisms collectively enhanced the immune response, resulting in ICD. Furthermore, **Ru-LND** significantly inhibits the growth of three-dimensional cell spheroids, demonstrating potential for the treatment of solid tumors. This paper has designed and synthesized a novel anticancer drug that combines photodynamic therapy with immunotherapy, providing a certain significance for the development of new metallodrugs.

4. Experimental

4.1. Synthesis of ligands and complexes

4.1.1. Synthesis of ligand N^N-LND (L2)

Under an argon atmosphere, LND (1 mmol, 321.4 mg) and EDCI (1.5 mmol, 287.6 mg) were dissolved in DMF (20 mL) and the solution was stirred for 20 min. Triethylamine was then added in a suitable amount, and the mixture was further stirred for an additional 20 min while maintained in an ice bath. HOBt (1.5 mmol, 202.7 mg) was introduced as a solid, and stirring was continued for another 20 min. Following this, 1,10-phenanthroline-5-amine (1.5 mmol, 292.5 mg) was incorporated, and the reaction mixture was stirred continuously for 48 h. Upon completion of the reaction, the solvent was evaporated under reduced pressure to yield a crude product, which was purified through flash column chromatography using a dichloromethane/methanol solvent system (40:1 ratio). The final product was obtained as a light yellow solid (268.9 mg, 54% yield). ^{1}HNMR (400 MHz, Chloroform-d) δ 9.48 (s, 1H), 9.26 (d, J = 4.3 Hz, 1H), 9.15 (d, J = 2.7 Hz, 1H), 8.71 (s, 1H), 8.48 (dd, J = 7.9, 27.2 Hz, 2H), 8.29 (d, J = 7.3 Hz, 1H), 7.75 (dd, J = 4.3, 8.4 Hz, 1H), 7.65 (dd, J = 4.3, 8.1 Hz, 1H), 7.54 – 7.43 (m, 3H), 7.19 (dd, J = 2.1, 8.3 Hz, 1H), 6.81 (d, J = 8.3 Hz, 1H), 5.80 (s, 2H), 5.31 (s, 1H).

*4.1.2. Synthesis of the complex [Ru(bpy)$_2$(L1)] 2PF$_6$ (**Ru-NH$_2$**)*

Under an argon atmosphere, cis-[Ru(bpy)$_2$Cl$_2$]·2H$_2$O (0.1 mmol, 53.0 mg) and 1,10-phenanthroline-5-amine (0.1 mmol, 48.3 mg) were dissolved in methanol (5 mL). The mixture was stirred at room temperature for 48 h. After the reaction was complete, the solvent was removed by rotary evaporation, and the crude product was treated with a saturated methanolic solution of NH_4PF_6. The product was purified by flash column chromatography (dichloromethane/methanol, 200:1) to afford the pure **Ru-NH$_2$** (76.4 mg, 85% yield). ^{1}HNMR (400 MHz, DMSO-d$_6$) δ 8.93-8.81 (m, 4H), 8.31 (d, J = 8.2 Hz, 1H), 8.22-8.05 (m, 6H), 7.84-7.81 (m, 3H), 7.58 (dd, J = 7.4, 13.4 Hz, 5H), 7.38 (q, J = 8.3 Hz, 2H), 7.09 (s, 1H), 6.93 (s, 1H), 2.89 (s, 1H), 2.73 (s, 1H).

*4.1.3. Synthesis of the complex [Ru(bpy)$_2$(LND)] 2PF$_6$ (**Ru-LND**)*

Under an argon atmosphere, cis-[Ru(bpy)$_2$Cl$_2$]·2H$_2$O (0.1 mmol, 53.0 mg) and N^N-LND (0.1 mmol, 49.7 mg) were dissolved in methanol (10 mL). The mixture was stirred at room temperature for 48 h. After the reaction was complete, the solvent was removed by rotary evaporation, and the crude product was treated with a saturated methanolic solution of NH_4PF_6. The product was purified by flash column chromatography (dichloromethane/methanol, 50:1) to afford the pure **Ru-LND** (102 mg, 85% yield). ^{1}HNMR (400 MHz, DMSO-d$_6$) δ 11.05 (s, 1H), 8.90-8.80 (m, 5H), 8.74 (d, J = 8.5 Hz, 1H), 8.65 (s, 1H), 8.27-8.08 (m, 7H), 7.93-7.85 (m, 5H), 7.76 (d, J = 2.1 Hz, 1H), 7.63-7.55 (m, 5H), 7.43-7.38 (m, 4H), 6.96 (d, J = 8.4 Hz, 1H), 5.98 (s, 2H). ESI-MS (positive mode, m/z): Calcd. 911.12, found 455.5.

Supporting Information

Supporting Information is available and includes synthetic and experimental procedures, ^{1}H NMR, ESI-MS, lipophilicity, UV-Vis absorption and fluorescence spectroscopy, mitochondrial membrane potential, apoptosis analysis,materials and methods, fluorescence measurements, photostability assessment, singlet oxygen detection, NADH detection, cytotoxicity in vitro, intracellular ROS production, cell survival rate, intracellular localization study, immunogenic cell death, western blotting assays, 3D tumor spheroids viability assays. Figures S1-S9, Scheme S1.

Conflict of Interest

The authors declare no conflict of interest.

Funding Information

This work was funded by the Original Exploration Program and General program of National Natural Science Foundation of China (Grant No. 22350001, 22077066, 22477062).

References

[1] Wu Y., Li S., Chen Y., He W., Guo Z., *Recent advances in noble metal complex based photodynamic therapy*, Chem. Sci., **13**, 2022, p. 5085-5106.
[2] Liu J., Zhang C., Rees T. W., Ke L., Ji L., Chao H., *Harnessing ruthenium(II) as photodynamic agents: Encouraging advances in cancer therapy*, Coord. Chem. Rev., **363**, 2018, p. 17-28.
[3] Shen J., Rees T. W., Ji L., Chao H., *Recent advances in ruthenium(II) and iridium(III) complexes containing nanosystems for cancer treatment and bioimaging*, Coord. Chem. Rev., **443**, 2021, p. 214016.
[4] Yang D., Lei S., Pan K., Chen T., Lin J., Ni G., Liu J., Zeng X., Chen Q., Dan H., *Application of photodynamic therapy in immune-related diseases*, Photodiagn. Photodyn. Ther., **34**, 2021, p. 102318.
[5] Ling Y. Y., Wang W. J., Hao L., Wu X. W., Liang J. H., Zhang H., Mao Z. W., Tan C. P., *Self-Amplifying Iridium(III) Photosensitizer for Ferroptosis-Mediated Immunotherapy Against Transferrin Receptor-Overexpressing Cancer*, Small, **18**, 2022, p. e2203659.
[6] Vigueras G., Markova L., Novohradsky V., Marco A., Cutillas N., Kostrhunova H., Kasparkova J.,

Ruiz J., Brabec V., *A photoactivated Ir(iii) complex targets cancer stem cells and induces secretion of damage-associated molecular patterns in melanoma cells characteristic of immunogenic cell death*, Inorg. Chem. Front., **8**, 2021, p. 4696-4711.
[7] Xu N., Zhang G.-D., Xue Z.-Y., Wang M.-M., Su Y., Fang H., Yu Z.-H., Liu H.-K., Lu H., Su Z., *NIR photoactivated electron intersystem crossing to evoke calcium-mediated lysosome-dependent cell death and immunotherapy*, Chem. Eng. J., **497**, 2024, p. 155022.
[8] Zeng Y. L., Liu L. Y., Ma T. Z., Liu Y., Liu B., Liu W., Shen Q. H., Wu C., Mao Z. W., *Iridium(III) Photosensitizers Induce Simultaneous Pyroptosis and Ferroptosis for Multi-Network Synergistic Tumor Immunotherapy,* Angew. Chem. Int. Ed., **63**, 2024, p. e202410803.
[9] Wang L., Karges J., Wei F., Xie L., Chen Z., Gasser G., Ji L., Chao H., *A mitochondria-localized iridium(iii) photosensitizer for two-photon photodynamic immunotherapy against melanoma*, Chem. Sci., **14**, 2023, p. 1461-1471.
[10] Deng Z., Wang N., Liu Y., Xu Z., Wang Z., Lau T. C., Zhu G., *A Photocaged, Water-Oxidizing, and Nucleolus-Targeted Pt(IV) Complex with a Distinct Anticancer Mechanism*, J. Am. Chem. Soc., **142**, 2020, p. 7803-7812.
[11] Xiong K., Wei F., Chen Y., Ji L., Chao H., *Recent Progress in Photodynamic Immunotherapy with Metal-Based Photosensitizers*, Small Methods, **7**, 2023, p. e2201403.
[12] Peng K., Zheng Y., Xia W., Mao Z. W., *Organometallic anti-tumor agents: targeting from biomolecules to dynamic bioprocesses*, Chem. Soc. Rev., **52**, 2023, p. 2790-2832.
[13] Imberti C., Zhang P., Huang H., Sadler P. J., *New Designs for Phototherapeutic Transition Metal Complexes*, Angew. Chem. Int. Ed., **59**, 2020, p. 61-73.
[14] Chen J., Tao Q., Wu J., Wang M., Su Z., Qian Y., Yu T., Wang Y., Xue X., Liu H. K., *A lysosome-targeted ruthenium (II) polypyridyl complex as photodynamic anticancer agent*, J. Inorg. Biochem., **210**, 2020, p. 111132.
[15] Zhou X., Zhu D., Liao Y., Liu W., Liu H., Ma Z., Xing D., *Synthesis, labeling and bioanalytical applications of a tris(2,2'-bipyridyl)ruthenium(II)-based electrochemiluminescence probe*, Nat. Protoc., **9**, 2014, p. 1146-1159.
[16] Lv M., Zheng Y., Wu J., Shen Z., Guo B., Hu G., Huang Y., Zhao J., Qian Y., Su Z., Wu C., Xue X., Liu H. K., Mao Z. W., *Evoking Ferroptosis by Synergistic Enhancement of a Cyclopentadienyl Iridium-Betulin Immune Agonist*, Angew. Chem. Int. Ed., **62**, 2023, p. e202312897.
[17] Lv M., Zheng Y., Dai X., Zhao J., Hu G., Ren M., Shen Z., Su Z., Wu C., Liu H. K., Xue X., Mao Z. W., *Ruthenium(ii)-Arene Complex Triggers Immunogenic Ferroptosis for Reversing Drug Resistance*, J. Med. Chem., **67**, 2024, p. 20156.
[18] Nath K., Guo L., Nancolas B., Nelson D. S., Shestov A. A., Lee S. C., Roman J., Zhou R., Leeper D. B., Halestrap A. P., Blair I. A., Glickson J. D., *Mechanism of antineoplastic activity of lonidamine*, Biochim. Biophys. Acta, **1866**, 2016, p. 151-162.
[19] Huang Y., Sun G., Sun X., Li F., Zhao L., Zhong R., Peng Y., *The Potential of Lonidamine in Combination with Chemotherapy and Physical Therapy in Cancer Treatment*, Cancers, **12**, 2020, p. 3332.
[20] Carloni P., Damiani E., Greci L., Stipa P., Tanfani F., Tartaglini E., Wozniak M., *On the use of 1,3-diphenylisobenzofuran (DPBF). Reactions with carbon and oxygen centered radicals in model and natural systems*, Res. Chem. Intermed., **19**, 1993, p. 395-405.
[21] Zhu S. Y., Yao R. Q., Li Y. X., Zhao P. Y., Ren C., Du X. H., Yao Y. M., *Lysosomal quality control of cell fate: a novel therapeutic target for human diseases*, Cell Death Dis., **11**, 2020, p. 817.
[22] Dondelinger Y., Declercq W., Montessuit S., Roelandt R., Goncalves A., Bruggeman I., Hulpiau P., Weber K., Sehon C. A., Marquis R. W., Bertin J., Gough P. J., Savvides S., Martinou J. C., Bertrand M. J., Vandenabeele P., *MLKL compromises plasma membrane integrity by binding to phosphatidylinositol phosphates*, Cell Rep., **7**, 2014, p. 971-981.
[23] Galluzzi L., Kepp O., Chan F. K., Kroemer G., *Necroptosis: Mechanisms and Relevance to Disease*, Annu. Rev. Pathol., **12**, 2017, p. 103-130.